Electronic Supplementary Information (ESI)

Insights into Charge Storage and Electroactivation of Mixed Metal Sulfides in Alkaline Media: NiCoMn Ternary Metal Sulfide Nano-needles Forming Core-Shell Structures for Hybrid Energy Storage

Jaime S. Sanchez,[a] Afshin Pendashteh,[a,b,*] Jesus Palma,[a] Marc Anderson,[a,c] and Rebeca Marcilla[a,*]

[a] Electrochemical Processes Unit, IMDEA Energy Institute, Avda. Ramon de la Sagra 3, Parque Tecnológico de Móstoles, 28935 Móstoles, Spain

[b] CIC Energigune, Parque Tecnológico de Álava, Albert Einstein 48 - ED. CIC 01510 Miñano, Spain.

[c] Department of Civil and Environmental Engineering, University of Wisconsin, Madison, USA.

* E-mail: apendashteh@cicenergigune.com, rebeca.marcilla@imdea.org

Electrochemical Measurements

The electrochemical behavior of the samples was first evaluated in a conventional three-electrode system using 3 M KOH as the electrolyte with a Bio-Logic VMP3 station through Cyclic Voltammetry (CV), Galvanostatic Charge-Discharge (GCD), and Electrochemical Impedance Spectroscopy (EIS) measurements. A platinum mesh and a Hg/HgO (1M NaOH,

ALS Co., Ltd Japan) electrode were employed as the counter and reference electrodes, respectively. The bare nickel foam was also tested, and a very small capacity was subtracted in calculating the specific capacities of the NCMS. In order to shed light on electroactivation process of the NCMS electrodes, ex-situ Raman and XRD studies were performed after applying potential pulses at 0.0, 0.3, and 0.6 V vs. Hg/HgO over 30 min. Raman and XRD spectra were also collected at different cycling numbers. Additionally, operando Raman test was also run on a JASCO NRS-5100 with a 20x objective lens. The exploration time was 50 second with twice sweeping for one spectrum and the voltage step was 0.15 V during two consecutive charge-discharge cycles at 2 mV·s^{-1}. We used low power (10 mW) of the 532 nm laser excitation to minimize the potential risks of photo-induced or thermal-induced structural changes of the electrode material.

In the case of two-electrode measurements, hybrid devices were assembled in Swagelok cells by sandwiching an impregnated cellulosic paper with the electrolyte (3 M KOH solution) between NCMS and rGO as the positive and negative electrodes, respectively. According to charge balance theory ($Q^+ = Q^-$), electrodes with a mass ratio (m^-/m^+) of 3.77 were used to assemble the devices. After assembly, hybrid devices were examined by CV, GCD and EIS measurements. Finally, cycling performance was tested over 5000 cycles at a specific current of 5 A·g^{-1}. Specific capacity of the samples was calculated from the CV and discharge curves according to the following equations:

$$Q_{sp} = \frac{\int Idt}{m} \quad ; \quad Q_{Areal} = \frac{\int Idt}{A} \tag{S1}$$

Where Q is the specific capacity (mAh·g^{-1} or mAh·cm^{-2}), I is the current, m is the mass of electrode material (g), A is the area of electrode material and dt is the time differential.

Specific energy (E_{sp}, Wh·kg^{-1}) and specific power (P_{sp}, W·kg^{-1}) were calculated from the discharge curves using the following equations:

$$E_{sp} = \frac{1}{m_t} \int I \cdot V \cdot dt \tag{S2}$$

$$P_{sp} = \frac{E_{sp}}{t_{discharge}} \tag{S3}$$

where E_{sp} (Wh·kg^{-1}) is specific energy, I (A) is the discharging current, V (V) is the potential, m_t (kg) is total mass of the electrode materials in negative and positive electrodes, P_{sp} (W·kg^{-1}) is the specific power and $t_{discharge}$ (h) is the time of discharge.

Power´s Law and Dunn´s method

To determine the different charge storage contributions of the electrochemical process involved, the power´s law was introduced:

$$i(V) = a \cdot V^b; \log i(V) = b \cdot \log V + \log a \tag{S4}$$

The current and the sweep rate obey a power-law relationship expressed as i= av^b, with the b-value providing insight into the charge storage mechanism. For a redox reaction confined by semi-infinite linear diffusion, the b-value would be 0.5; for a surface-controlled process, the b-value would be 1. Moreover, the b value could act as an indicator for differentiating pseudocapacitor-type from battery-type materials. On the other hand, the ability to decompose the total current into contributions from faradaic capacity and double layer capacitance is critically important in terms of providing an understanding of the charge-storage mechanisms that are operating; in this regard Dunn´s method was introduced:

$$i(V) = K_1 \cdot v + K_2 \cdot v^{1/2}; \frac{i(V)}{v^{1/2}} = K_1 \cdot v^{1/2} + K_2 \tag{S5}$$

By calculating both k_1 and k_2 constants, we can extract the fraction of the current from capacitance and diffusion.
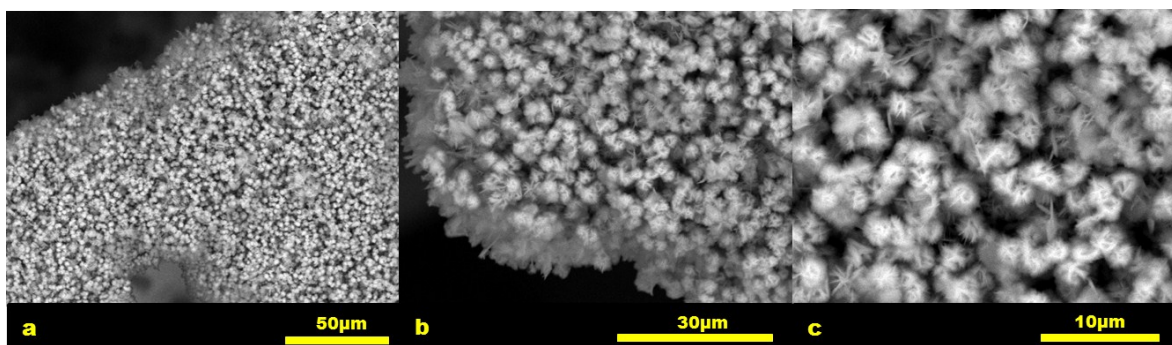

Figure S1. SEM micrographs of the $(Ni_{1-(x+y)}Co_xMn_y)OH_2$ urchin-like structure supported on Ni foam at different magnifications.

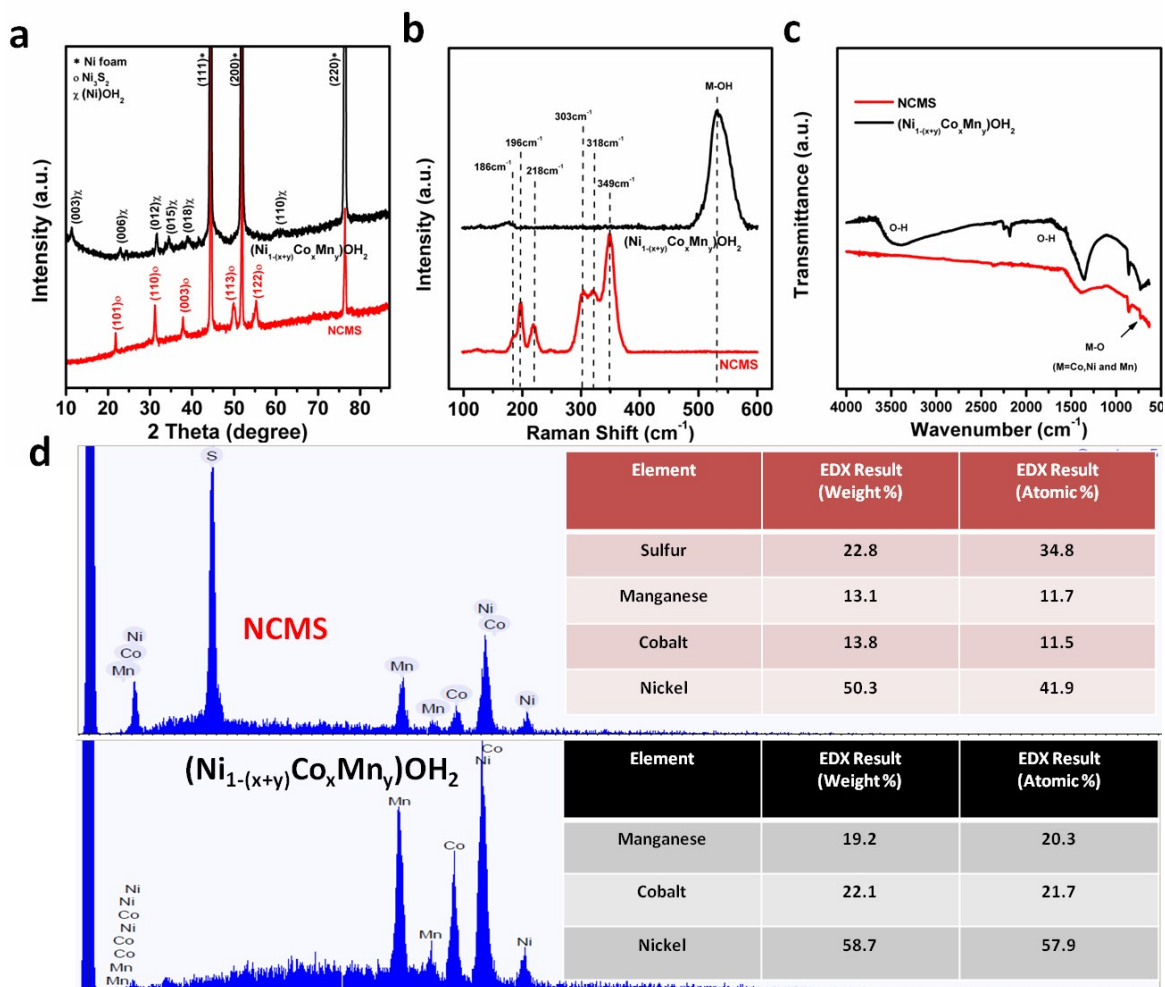**Figure S2**. (a) XRD of the NCMS and $(Ni_{1-(x+y)}Co_xMn_y)OH_2$ samples including the corresponding hkl planes; three sharp peaks corresponding to Ni foam are marked with asterisks (b) Raman Spectra of the NCMS and $(Ni_{1-(x+y)}Co_xMn_y)OH_2$ samples (c) FTIR Spectra of the NCMS and $(Ni_{1-(x+y)}Co_xMn_y)OH_2$ samples (d) EDX spectrum of the NCMS and $(Ni_{1-(x+y)}Co_xMn_y)OH_2$ samples.
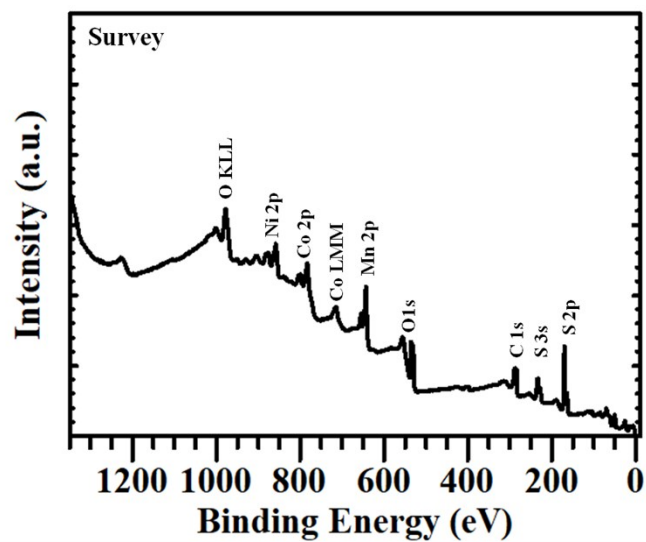
Fig. S3. XPS Survey Spectra for NCMS sample

Table S1. Valence states of Ni, Co and Mn in NCMS sample.

Sample	Ni^{2+}/Ni^{3+}	Co^{2+}/Co^{3+}	Mn^{2+}/Mn^{3+}	Ni^{x+}	Co^{y+}	Mn^{z+}
NCMS	3.53	4.68	5.19	x=2.22	y=2.19	z=2.15
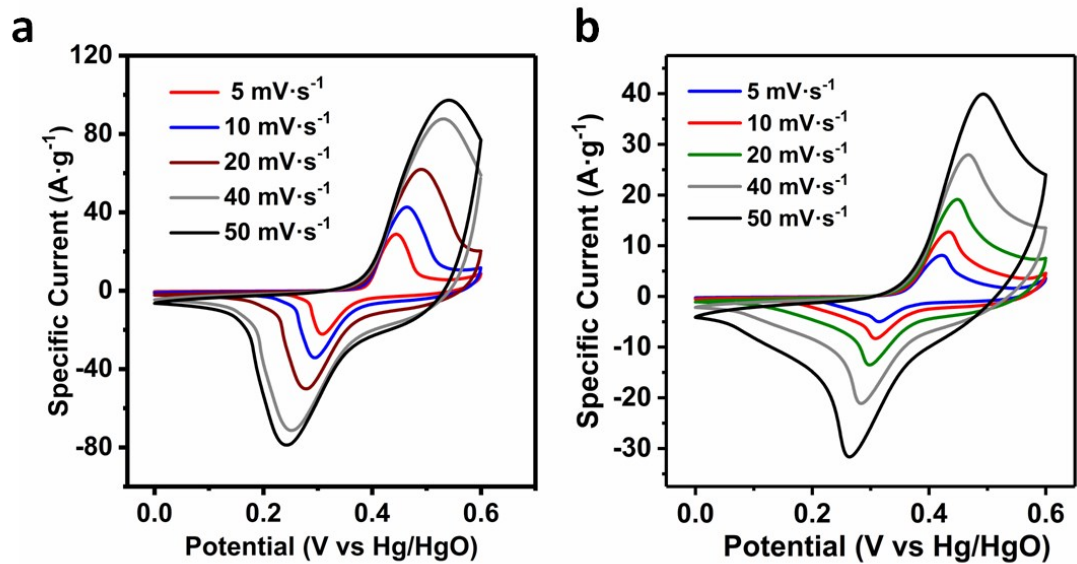
Figure S4. (a) CV curves of the NCMS nano-needle and (b) $(Ni_{1-(x+y)}Co_xMn_y)OH_2$ sample at various scan rates
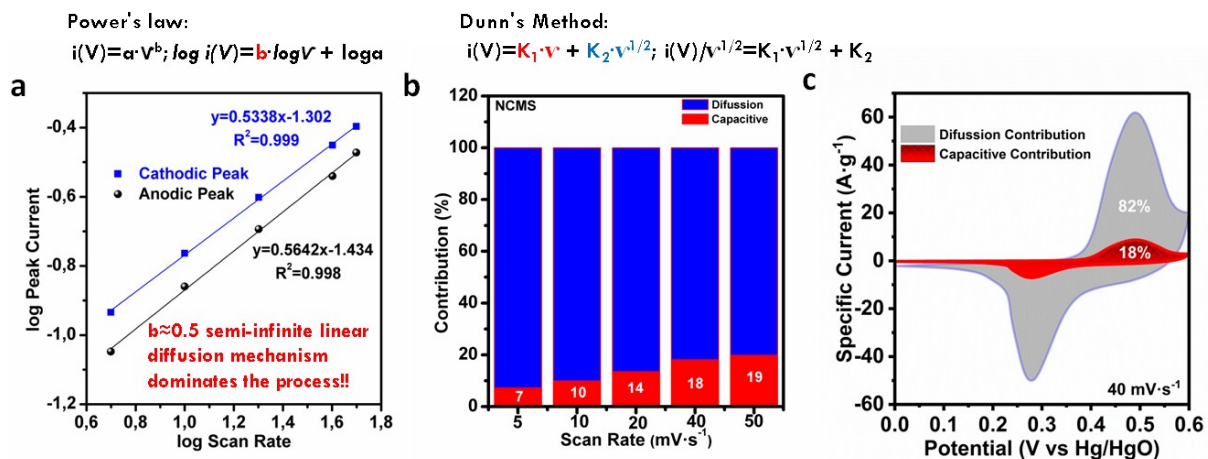
Figure S5. (a) Variation between log(i) vs. log (scan rate) for Power's law from the CV curves of NCMS (b) contribution percentages for diffusion-limited process and capacitive process for scan rates 5 to 50 mV·s⁻¹ in NCMS electrode (c) capacitive and diffusion-controled contribution to charge storage at 40 mV·s⁻¹.
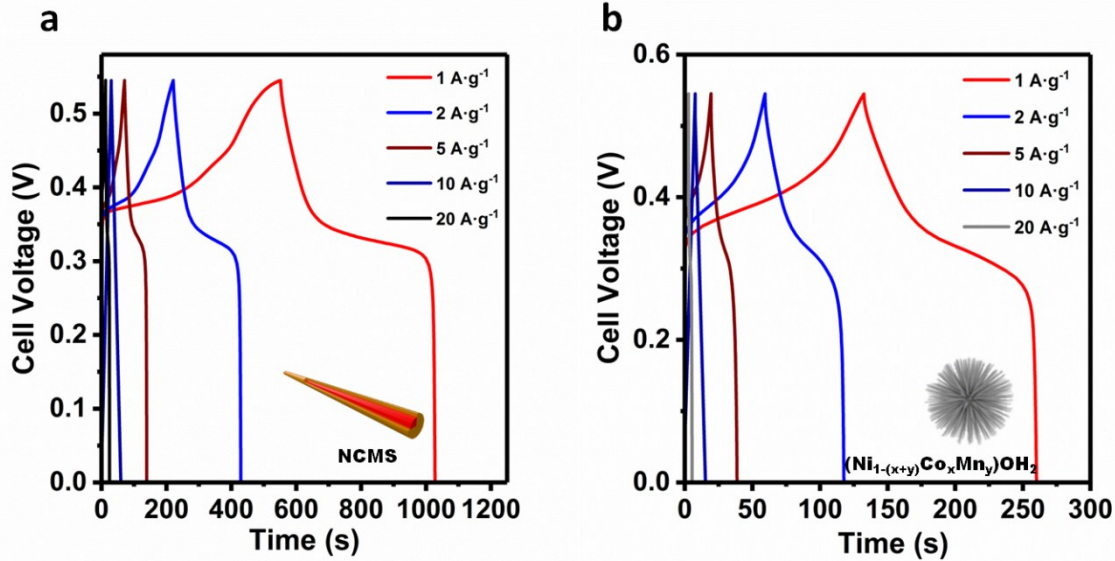
Figure S6. Galvanostatic charge-discharge curves of the as-prepared NCMS nano-needle structure (a) and $(Ni_{1-(x+y)}Co_xMn_y)OH_2$ urchin-like structure (b) at different current densities.
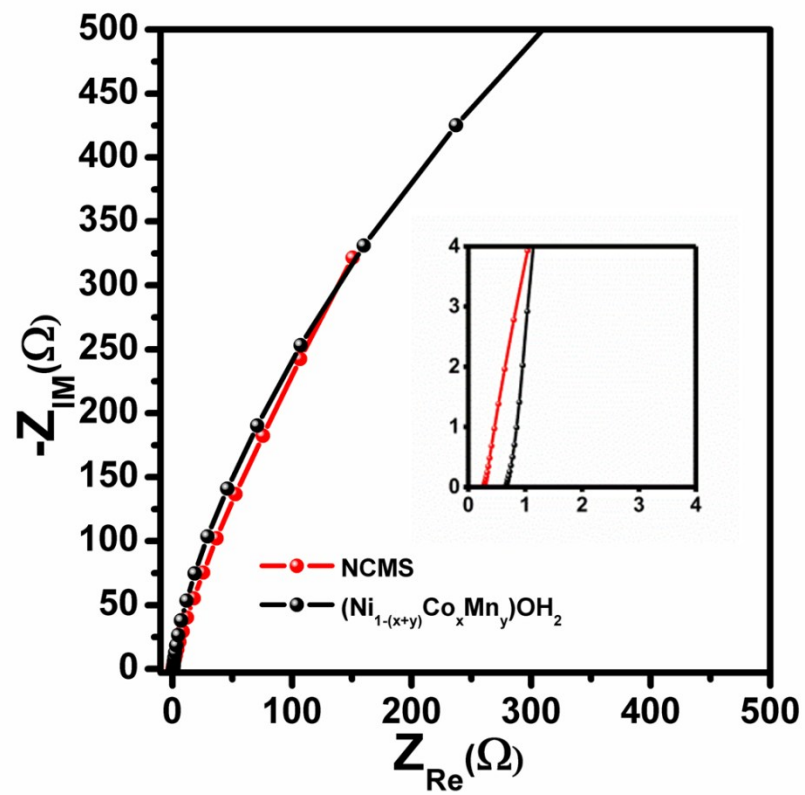
Figure S7. Nyquist Plot of the as-prepared NCMS and $(Ni_{1-(x+y)}Co_xMn_y)OH_2$.
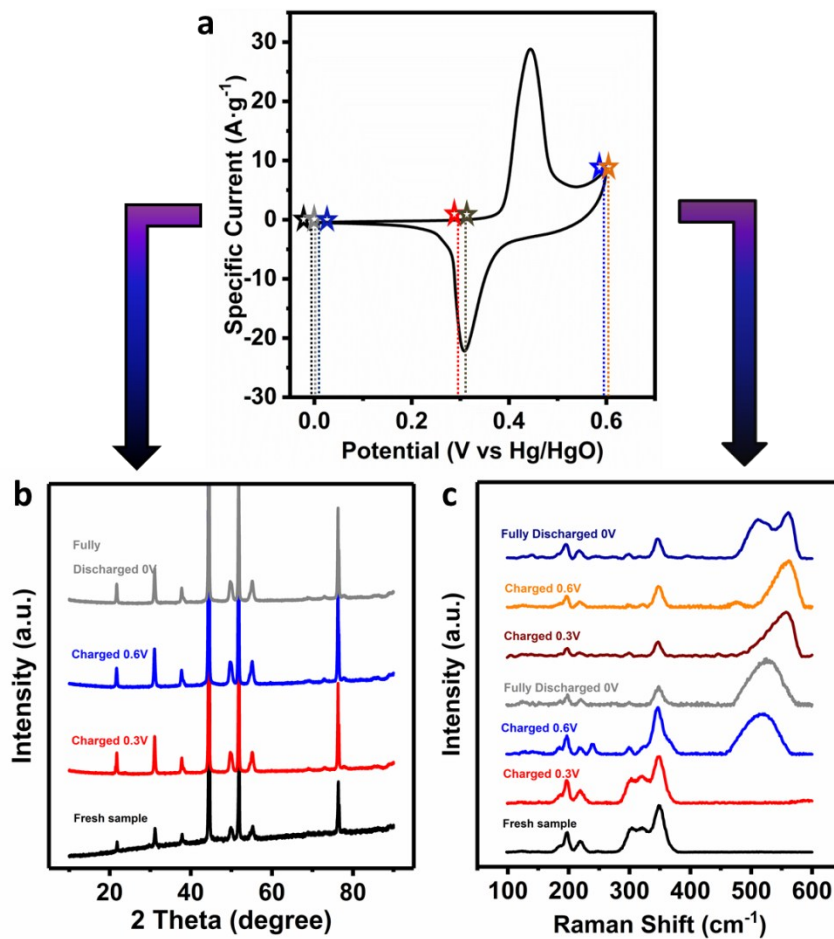
Figure S8. (a) CV curve of NCMS with various ex-situ points marked at different states of charge (b) XRD of the NCMS sample at different states of charge (c) Raman spectra of the NCMS sample at different states of charge.
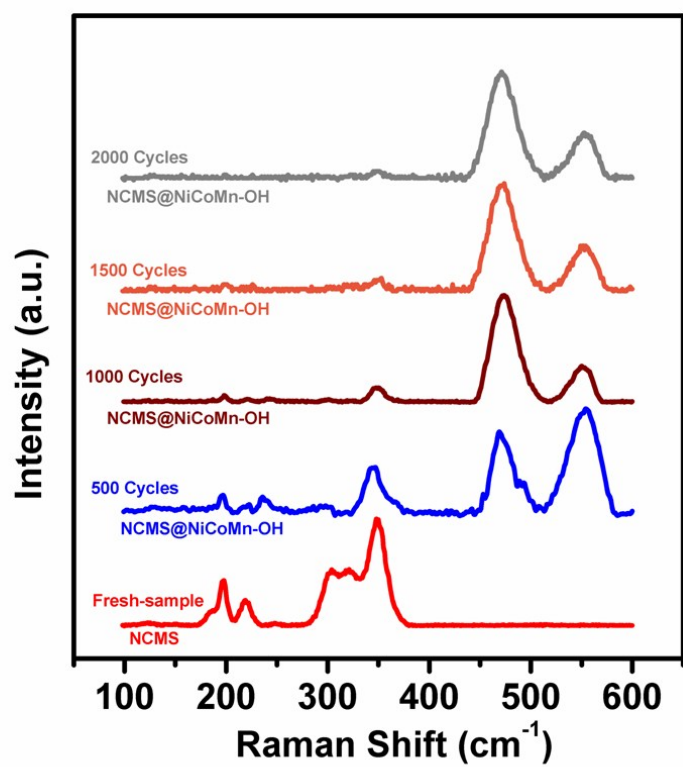
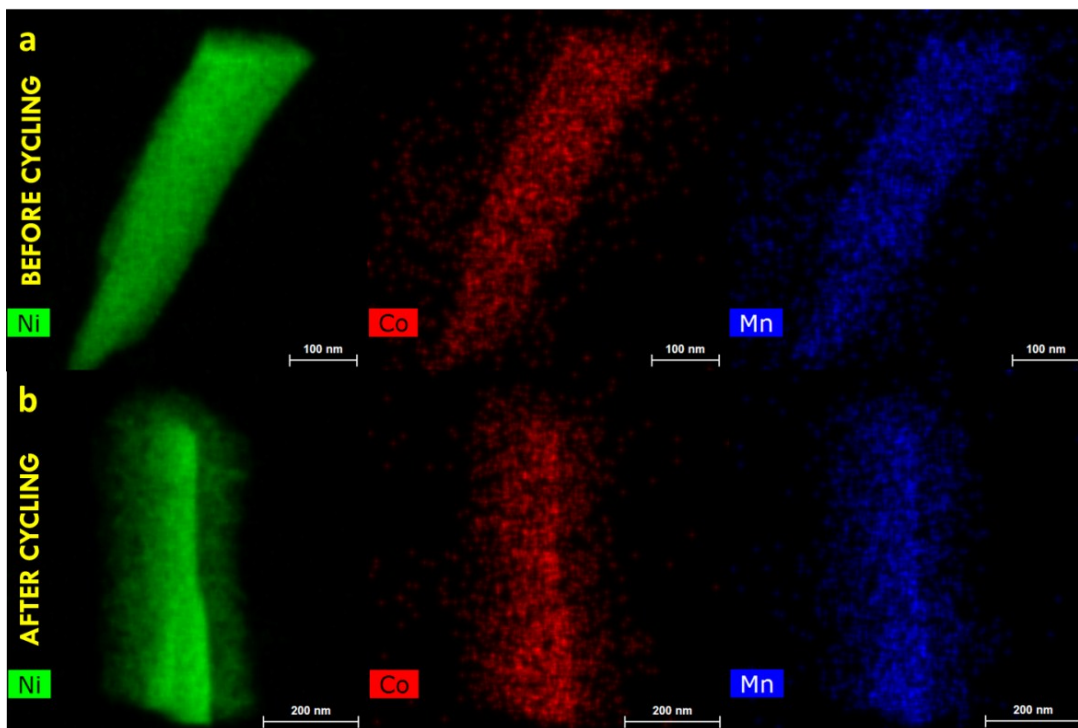**Figure S9.** Raman spectra of the NCMS@NiCoMn-OH at different cycle numbers.

Figure S10. (a) STEM elemental maps of Ni, Co and Mn before cycling, (b) STEM elemental maps of Ni, Co and Mn after cycling.
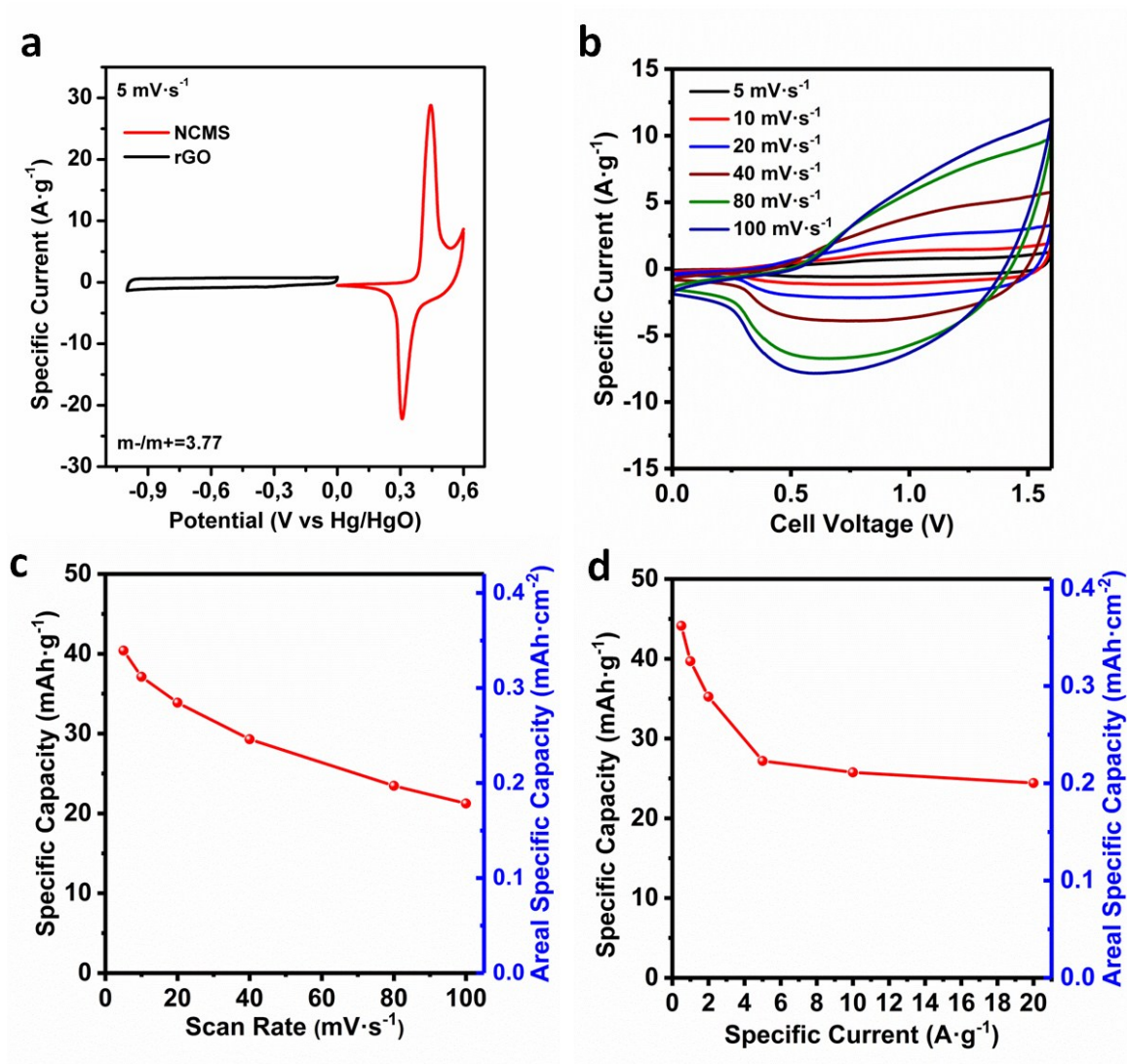
Figure S11. (a) CV curves of the negative rGO and positive NCMS in three-electrode configuration (b) CV curves of the rGO NSs// NCMS hybrid device at different scan rates (c) Rate capability of the rGO NSs//NCMS hybrid device at different scan rates (d) Rate capability of the rGO NSs//NCMS hybrid device at different current densities.
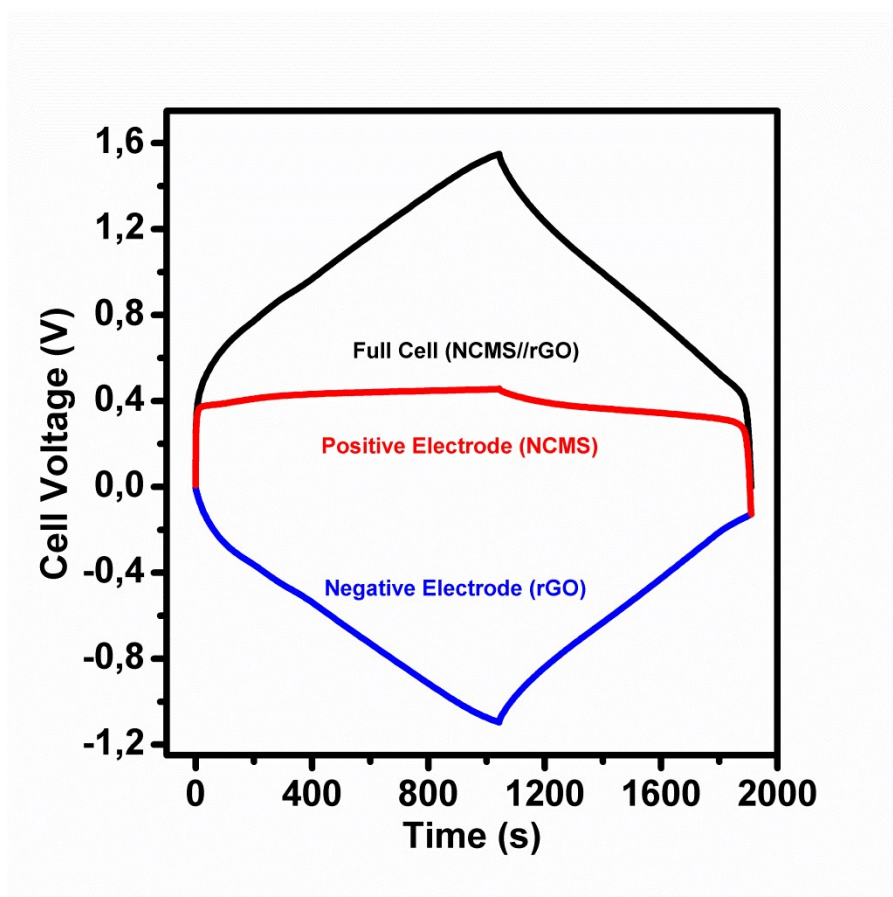
Figure S12. Behavior of individual electrodes in the full cell (NCMS//rGO) monitored via a Hg/HgO reference electrode placed in a T-shape Swagelok® cell at a discharge current density of 0.25 A·g⁻¹.
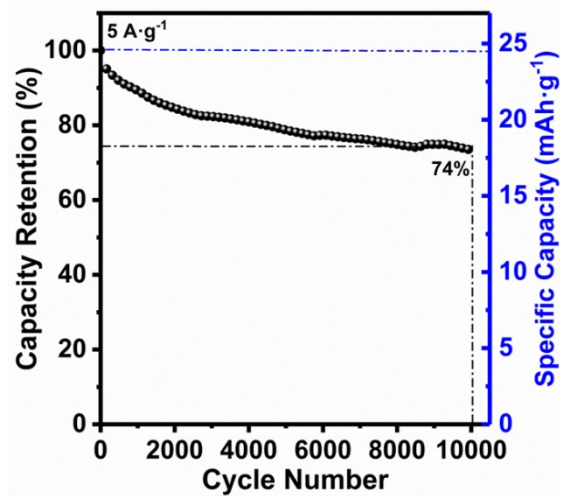
Figure S13. Cycling performance of the NCMS//rGO NSs hybrid device at a specific current

of 5 A·g^{-1} after 10000 cycles